Received March 7, 2020, accepted March 25, 2020, date of publication April 13, 2020, date of current version May 4, 2020.

Digital Object Identifier 10.1109/ACCESS.2020.2987618

Universal Kriging Prediction of Line-of-Sight Microwave Fading

STEPHEN J. SALAMON, (Member, IEEE), HEDLEY J. HANSEN, (Member, IEEE), AND DEREK ABBOTT, (Fellow, IEEE)

School of Electrical and Electronic Engineering, The University of Adelaide, Adelaide, SA 5000, Australia

Corresponding author: Stephen J. Salamon (stephen.salamon@adelaide.edu.au)

ABSTRACT Prediction of the severity of multipath fading is fundamental to the design of point-to-point terrestrial fixed microwave links at frequencies below 10 GHz, but error in this prediction may be significant in countries such as Australia, not represented in the dataset used to generate existing empirical models. We take advantage of recently collected worst-month fading data from Australia, and find new parameters particularly useful in predicting the severe fading experienced in Northern Australia. These parameters are from very irregularly spaced weather stations, so we investigate various interpolation techniques for this situation, including a new version of natural neighbour interpolation. Conventional multipath prediction models are based on ordinary least squares (OLS) regression, but we refine this, taking spatial correlation into account with generalised least squares (GLS) regression. We then demonstrate further improvement in regions well populated by measured data, by employing universal kriging.

INDEX TERMS Fading channels, interpolation, least squares approximation, microwave propagation, radiowave propagation, regression analysis.

I. INTRODUCTION

Terrestrial microwave radio links have been a significant component of communication networks for over half a century, and empirical models to predict the clear-air fading events (not associated with rain) that they occasionally suffer, have been of interest to radio link designers for most of that time. Optical fibre has largely replaced digital radio on most major long routes in the transmission network, but digital radio is still important on routes where optical fibre is uneconomical, such as off-shore islands, or niche applications such as low-latency networks.

Radio link design depends on accurate estimation of the severity of fading events, as this determines the required design fade margin. This is the attenuation of received signal, compared to median conditions, which may be tolerated before serious transmission errors occur. Increasing the system fade margin is expensive as it involves costs such as increased antenna size and stronger support structures, but insufficient fade margin leads to poor link error performance. Above 10 GHz rain attenuation tends to dominate terrestrial radio link fading, but below 10 GHz clear-air fading, the subject of this study, tends to dominate.

The associate editor coordinating the review of this manuscript and approving it for publication was Vittorio Degli-Esposti.

A. EARLY HISTORY OF CLEAR-AIR FADING MODELS

It has long been recognised that multipath propagation, due to variations in the refractive index of the air at different heights in the surface layer of the atmosphere, is a significant factor in fading of microwave paths [1]. During fading events, the signal strength tends to be Rayleigh distributed, or in other words, the tail of the fading distribution for small percentages of time tends to have a slope of 10 dB per decade of probability. The deep-fading distribution may be estimated in terms of a slope of 10 dB per decade of probability relative to the fade depth (dB) for 0.01% of the worst month of an average year, $A_{0.01}$, and this formulation is used throughout this paper. Based on measurements in the United Kingdom, Pearson [1] suggested a prediction model, in terms of distance d (km) and path roughness s (m), which may be written as

$$A_{0.01} = 27.8\log(d) - 12.37\log(s) + 2.43 \text{ dB}. \quad (1)$$

Another early example by Morita [2], had separate models, depending on the terrain or climate type. Expressed in a similar form to (1), the version provided in [3] is, firstly for inland paths:

$$A_{0.01} = 12\log(f) + 35\log(d) - 30 \text{ dB}, \quad (2)$$

or mountainous paths:

$$A_{0.01} = 12\log(f) + 35\log(d) - 34.09 \text{ dB}, \quad (3)$$

or coastal paths, temperate and fairly flat:

$$A_{0.01} = 12\log(f) + 35\log(d) - 5\log(h_1 + h_2) - 10.04 \text{ dB}, \quad (4)$$

where f is the frequency (GHz), and h_1, h_2 are terminal antenna heights (m) above mean sea level.

Well known is the Barnett-Vigants model [4], [5], again consisting of different versions, depending on the terrain or climate. For "average terrain":

$$A_{0.01} = 10\log(f) + 30\log(d) - 22.22 \text{ dB}, \quad (5)$$

or over-water or Gulf Coast:

$$A_{0.01} = 10\log(f) + 30\log(d) - 16.2 \text{ dB}, \quad (6)$$

or mountains or dry climate:

$$A_{0.01} = 10\log(f) + 30\log(d) - 28.24 \text{ dB}. \quad (7)$$

Although expressed above logarithmically in terms of fade depth for 0.01% of the worst month, the above models are often expressed in a power-law form, in terms of percentage p of the worst month that the fade depth exceeds A dB. Thus the Barnett-Vigants model may be written [3] as

$$p = KQfd^3 10^{-A/10} \quad (8)$$

where K is a factor representing the effect of terrain and climate, and Q is a factor accounting for the effect of path variables other than d and f. We use the equivalent logarithmic form of the models in this paper, for simplicity in later discussion of multiple linear regression models.

Terrain roughness, or standard deviation of terrain height along the radio path, s, was taken into account in a later version of the US or Barnett-Vigants model, given in [3]; we note the similarity of the following to (1) around 4 GHz. In the case of coastal or over water paths:

$$A_{0.01} = 10\log(f) + 30\log(d) - 13\log(s) - 3.87 \text{ dB}, \quad (9)$$

or maritime subtropical:

$$A_{0.01} = 10\log(f) + 30\log(d) - 13\log(s) - 5.09 \text{ dB}, \quad (10)$$

or inland:

$$A_{0.01} = 10\log(f) + 30\log(d) - 13\log(s) - 6.78 \text{ dB}, \quad (11)$$

or mountainous:

$$A_{0.01} = 10\log(f) + 30\log(d) - 13\log(s) - 10 \text{ dB}. \quad (12)$$

A fundamental problem with the above models (2) to (12), is the need to choose a version of the model, based on the subjective assessment of the terrain or climate type. This problem remained in the ITU-R prediction model until 1999 [6], [7], as the model contained constants to be chosen according to terrain type (plains, hills or mountains). Comparative testing of the above models is provided in [8].

B. MEDIAN DEPRESSION FADING

During multipath fading events, a depression in the median signal level is often seen. An early description [1] was that "median depression during worst fading hour is approximately 0.3 × fade depth for 0.1% of the worst month." This reference, based on experience in the United Kingdom, even reported "almost complete loss of signal (space-wave fadeout) that can occur on some paths."

One possible cause identified for median depressions was positive vertical gradients of radio refractivity in the atmosphere, known as *subrefraction*. The upward curvature of ray-paths caused by a linear gradient of this type, if sufficiently severe, may be expected to cause terrain obstruction of a radio link that is normally unobstructed. A ray-path between transmitter and receiver when there is a positive refractivity gradient will travel closer to the ground than the *standard refractivity* case of mildly negative vertical gradient.

Radio refractivity is normally expressed in "N-units," or parts per million by which atmospheric refractive index for radio waves exceeds unity. Thus, vertical refractivity gradients are expressed in N-units per km. Standard refactivity for terrestrial radio links is typically assumed to be a gradient of –39 N-units per km.

The refractivity N is estimated as proportional to the partial pressures of various gas constituents of the atmosphere and inversely proportional to absolute temperature T, except that in the case of water vapour pressure e, there is another term inversely proportional to absolute temperature squared, due to the polar nature of the water molecule. Expressed simply, with total air pressure P, consisting of dry air pressure $P - e$ and water vapour pressure e, we have, for example, the Bean model [9]

$$N = 77.6\left(\frac{P-e}{T}\right) + 72\frac{e}{T} + 375000\frac{e}{T^2}, \quad (13)$$

or the more recent Rueger "best average" model [10]

$$N = 77.689\left(\frac{P-e}{T}\right) + 71.295\frac{e}{T} + 375463\frac{e}{T^2}. \quad (14)$$

While non-linear gradient refractive effects, such as focussing or de-focussing, or even caustics that cause ray-paths from the transmit antenna to miss the receive antenna entirely [11], may cause median depression fading, a simple model for the worst subrefractive gradient likely to be experienced in a temperate climate [11] has been employed as part of clearance criteria for line-of-sight path design for many years [3], [6], [12]. This model depends on radio path length d (km), and may be expressed as a vertical refractivity gradient:

$$\frac{dN}{dh} = \frac{2670}{d} - 13 \quad \text{N-units per km}. \quad (15)$$

However, more severe median depression fading has been observed in some regions; for example, the coastal region of the Nullabor Plain in southern Australia [13], inland Queensland in north-eastern Australia [14], or south-eastern

USA [15], [16]. A common feature of these studies is the assumption that a linear positive refractivity gradient is the likely worst-case of a subrefractive atmosphere. Boundary layer similarity theory [17] indicates that surface refractivity gradients are likely to be stronger near the surface than at greater heights, and a subrefractive profile of this non-linear form has been shown to be capable of greater attenuation on a terrestrial path than a linear gradient with the same increase in refractivity over the lowest 100 m of the atmosphere [18].

Nevertheless, the idea of complementing a multipath fading model with a subrefractive diffraction model [16] has been often adopted as a convenient way to estimate the overall fading of radio paths in regions where the available multipath models alone are insufficient. The necessary data for the Schiavone model [15] has been produced for the contiguous states of USA [19], but not for other regions. A subrefractive model, assuming the main cause to be advection of moist air over a dry nocturnal duct, during the early hours of the morning [14], may in principle be applied world-wide, subject to the availability of suitable (preferably 3-hourly or better) surface weather station data.

C. MEDIAN DEPRESSION, MULTIPATH, AND DIVERSITY

During the minimum signal conditions in median depression events, received signal fluctuation suggests that multipath is occurring, and this tends to be supported by a fading distribution slope of about 10 dB per decade in the region of 0.1% of the worst month, for the severe median depression fading 7.5 GHz path from Cooks Tank to Rosewood in Queensland, Australia [20]. The worst median depression in this month on that path, with a depth of about 50 dB, cannot be created by multipath cancellation alone, as all four receivers, on two different frequencies for the two directions of transmission, and with receiver antennas at two different heights at each terminal, all experience the deep median depression at the same time. This characteristic is generally seen in other median depression events on other radio paths.

These characteristics suggest that on line-of-sight microwave paths, severe multipath fading and median depression tend to occur together, as parts of a continuum, rather than distinct events. This is inherent in the ITU-R multipath model [12], since the multipath occurrence factor P_0 (intercept of the extrapolated deep fading distribution with the zero dB or time axis) is generally greater than the multipath activity parameter η, the proportion of the time that multipath is assumed to be occurring. In the model [12], the two are related by the expression

$$\eta = 1 - \exp(-0.2P_0^{0.75}). \tag{16}$$

Radio links often employ diversity reception to reduce errors and outage during multipath fading, using two or more receivers with different antenna heights (space diversity) or receiving a second transmission on a different frequency (frequency diversity), taking advantage of their partially correlated multipath fading. Provided the depth of the median depression is less than the system fade margin, there may still be some diversity improvement during median depression fades, albeit quite limited. The median depressions are generally simultaneous between the different receivers, but the superimposed multipath is likely to de-correlated to some extent. A recent revision of the diversity improvement models in Recommendation ITU-R P.530 [12] has ensured that fading severity is taken into account in all diversity improvement models, to reflect the degradation in all types diversity improvement seen during severe median depression fading events.

D. DEVELOPMENTS IN THE LAST TWO DECADES

1) THE ATMOSPHERIC PHYSICS APPROACH

The fading prediction models described above were empirical, rather than scientific. A potential atmospheric physics approach may be to predict the state of the atmosphere with a numerical weather prediction (NWP) model, and then use a terrain parabolic equation model (PEM) [21], [22] to predict the radio propagation. This idea has been pursued for some time, both for radio link propagation [23], and in radar propagation research, but sub-meter resolution may be required in generating the refractivity profile [24]. An NWP reanalysis product with at least several years of data at very high resolution would be required, to practically implement fading prediction for path design, using this approach. Even then, the link designer would have to run a few years equivalent of PEM simulations, to accurately determine the average year worst month performance of the link; despite advances in computing capability, this still seems rather impractical.

There is doubt about the accuracy of radio refractivity predictions in the surface layer using existing NWP models in some locations [25]. In that study, a relatively simple empirical model provided better accuracy than NWP reanalysis data, in predicting surface refractivity gradient cumulative distributions. Testing of surface layer gradient accuracy, perhaps particularly water vapour pressure gradient accuracy, would be required before adopting a new NWP for radio path fading prediction.

2) MULTIPLE LINEAR REGRESSION

A significant advance came with the development of ordinary least squares (OLS) regression models, using as many parameters as were found to be practically useful [26]. By this time, 265 records had been accumulated in the ITU-R line-of-sight link fading databank, DBSG3 Table I-2 [27], "Line-of-sight average worst-month multipath fading and enhancement in narrow bandwidths," and 251 of those were found to be suitable for the regression analysis. As well as additional observed fading records, several new prediction parameters had been added since an earlier study with only 47 observed records [28]. A progressive approach was now used in selecting prediction parameters; the one with greatest positive or negative correlation with the observed fading selected first, and an OLS regression model generated. The next parameter chosen was that with strongest correlation with the residuals

(observed minus predicted) from the previous model, and a new regression model produced. This process was continued until further improvements in the model accuracy became minimal.

Most early prediction models, such as (2) to (12) above, included link frequency in the form $a\log(f)$, or $f^{a/10}$ in the power-law form of (8). Despite the 251 databank records then available, $\log(f)$ did not appear to be a significant parameter in the regression analysis; f was statistically more significant, so based on this work, the ITU-R prediction model was amended [29] to

$$A_{0.01} = 32\log(d) - 9.2\log(1+|\epsilon_p|) - 4.2\log(s_a) + 0.32f - 0.03dN_1 - 0.0085h_L - 39 \text{ dB}, \quad (17)$$

where ϵ_p is the path inclination in mr, h_L is the height above sea level of the lowest antenna, s_a is terrain elevation standard deviation (m, over a 1 degree latitude by 1 degree longitude square), and dN_1 is the 1% point of the cumulative distribution of refractivity gradient in the 65 m surface layer from 2 years of NWP reanalysis data from the European Centre for Medium-range Weather Forecasting (ECMWF).

Although not evident from the OLS regression analysis, there was concern that the model variation between 1 GHz and 10 GHz (3 dB) was insufficient, while the increase in model prediction between 10 GHz and 80 GHz (22 dB) appeared to be excessive. Accordingly, it was decided, and internationally agreed, to amend the frequency term [30] to $8\log(f)$. Clearly there was a need for more data from links in different frequency bands in the databank, to clarify the choice of frequency coefficient in future models.

More data records were added to the DBSG3 table, 3 from Turkmenistan and 8 from Kyrgyzstan in 2007. Then a technique was developed in Australia to produce monthly fading distributions from installed radio links, by estimating the cumulative distribution in each 15 minute period from observed maximum and minimum receive levels, and number of seconds below certain thresholds [20]; data that was being routinely captured by the network management system. This enabled average-year worst-month fading distributions to be produced for many links, without the cost of installing additional monitoring equipment. By 2016, 70 records from Australia had been produced, all in the 7.5 and 8 GHz bands. Additional information on processing this data from small and medium capacity systems to avoid the influence of selective fading is given in [31], and summarised in Appendix A. A new OLS model was developed, for the first time including a number of records from Australia [32].

A similar process to that described above for [26] was used to select variables for the OLS regression, but as well as new data records (there were now 327), we added new prediction parameters, obtained from surface weather station data. Two were composite parameters v_1 and v_2, given by

$$v_1 = \frac{N_{sA90-10}^{0.3} d^{0.5}}{H_{8500}^{0.25}}, \text{ and} \quad (18)$$

$$v_2 = \frac{dN_{75\text{mH}}^3}{H_{8500}^2}, \quad (19)$$

where H_{8500} is the mean height of the rayline above the terrain (at standard refractivity gradient or -39 N-units per km, ignoring tree cover, if any). The Harvey [14] 75 m point subrefraction (we assume for 0.1% of the worst month of the year) is $dN_{75\text{mH}}$, while $N_{sA90-10}$ and $N_{sA0.1}$ are the interdecile range and 0.1% point respectively of the distribution of surface refractivity anomaly, the difference between surface refractivity and the median value at that location for the same hour of the day and month of the year. In that study [32], these parameters $dN_{75\text{mH}}$, $N_{sA90-10}$, and $N_{sA0.1}$, were obtained from surface weather station data for the years 2012 to 2014. The resulting OLS regression model was

$$A_{0.01} = 2.04v_1 + 0.0679v_2 + 17.71\log(d) - 0.171N_{sA0.1} - 9.06\log(1+|\epsilon_p|) - 0.0278dN_1 + 0.0374dN_{1\text{ERAI}} + 7.41\log(f+6) - 0.003h_L - 19.63 \text{ dB}, \quad (20)$$

This OLS model had much better accuracy than the existing ITU-R model [12] for the post-2007 links that were not included in fitting that model, and similar accuracy as before for the ones that were included in fitting that model. The $\log(f)$ term still appeared insignificant, but $\log(f+6)$ was found to be significant.

It was suspected that the statistical significance attributed to some of the parameters in this new model by the t-statistic may have been inflated, so we investigated taking spatial correlation into account, by using generalised least squares (GLS) regression instead of OLS regression [33]. This analysis confirmed that parameter $dN_{1\text{ERAI}}$, nominally the same parameter as dN_1 but from a more recent and much more extensive ECMWF reanalysis [34], was not significant after all.

E. ORGANISATION OF THIS PAPER

In the following sections we examine techniques for spatial interpolation of parameters obtained from surface weather station data, and then describe a new GLS regression model, taking advantage of additional link fading data now available. Accurate guidance to designers on the improvement provided by increased antenna height is important, so we test that aspect of the new model.

Finally we introduce a new technique in fading prediction — universal kriging. This combines GLS regression with interpolation of residuals from nearby links with known fading, to improve the accuracy of predictions in regions well populated with observed fading data.

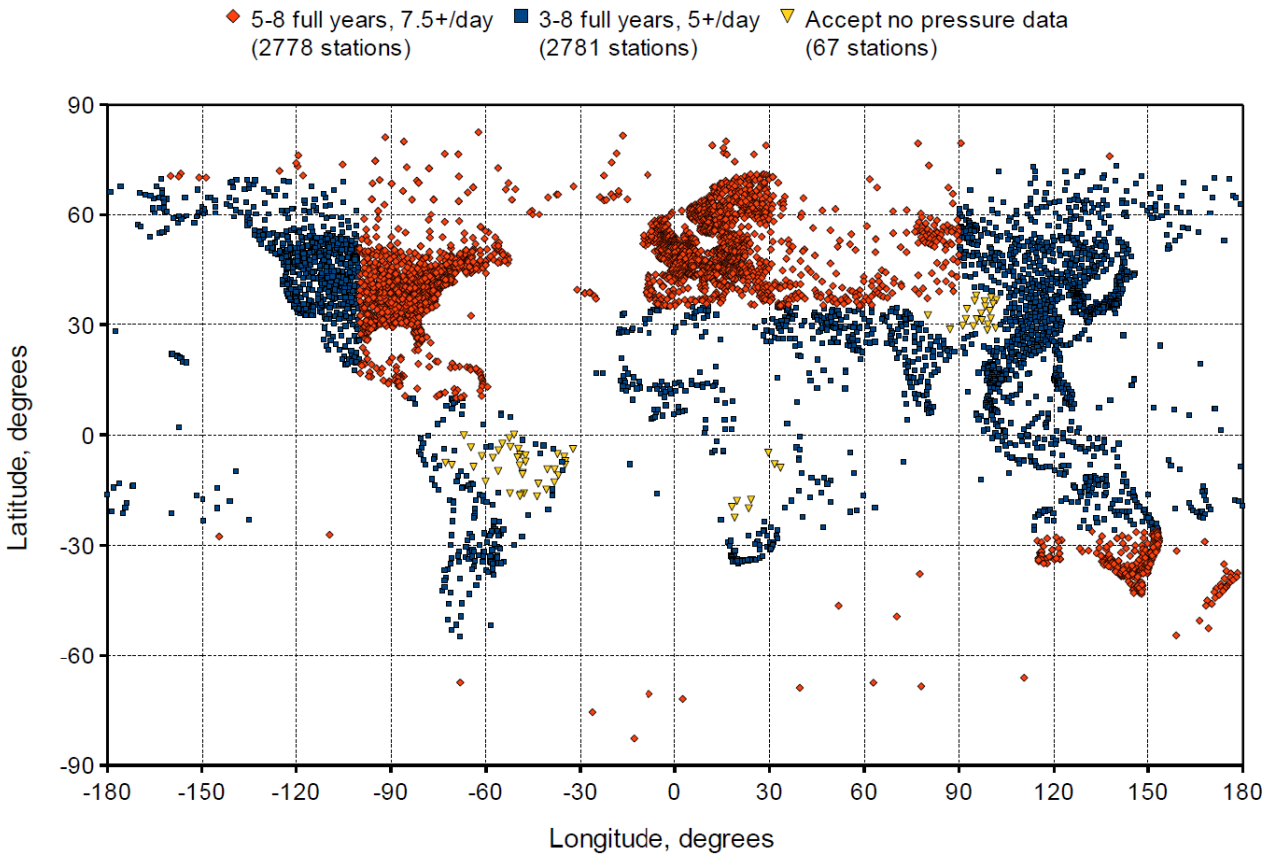

FIGURE 1. Surface weather stations, showing regions with many stations (red diamonds), less stations (blue squares), and 67 with no pressure data (yellow triangles).

II. DATA SOURCES

A. PARAMETERS FROM WEATHER STATIONS

The surface weather station data is obtained from the NOAA FTP site [35], for the eight years 2010 to 2017. In regions with a relatively dense population of stations having temperature, humidity, and air pressure data, we included those with 7.5 or more measurements per day in every month for at least 5 full years; there were 2778 stations in those regions. Elsewhere, we included stations with at least 3 full years of data, and 5 or more measurements per day; this provided a further 2781 stations. There remained extensive regions in three continents with no data, due to an absence of air pressure data, so a further 67 stations with only temperature and humidity data were included. For these stations a nominal sea-level pressure of 1000 hPa is assumed. All station pressures were estimated from sea-level pressures by assuming a lapse rate of -0.12 hPa per m.

Overall, 5626 surface weather stations are included in generating the digital maps used in this study, as depicted in Fig. 1.

B. RADIO LINK FADING DATA

The link fading data consists of 409 records from the most recently accepted data table the ITU-R line-of-sight link fading databank, DBSG3 Table I-2 [27], "Line-of-sight average worst-month multipath fading and enhancement in narrow bandwidths," after excluding 48 of the total 457 records because of data inconsistencies, or absence of one or more parameters required for this study. To this we add 126 recently generated Australian records, not yet considered by ITU-R Study-Group 3 for inclusion in the DBSG3 databank, resulting in a total of 535 data records for this study.

We divide these records into 20 regions, each including links within 1500 km of centre coordinates, chosen initially for each region as the link centre coordinates of the first link encountered that falls outside the 1500 km radii of regions already defined, and then updated to the median coordinates as more links are added to each region. The details of these regions are shown in Table 1.

C. POTENTIAL IMPACT OF CLIMATE CHANGE

Direct observation of a trend in average year worst month fading is not possible because worst month fading data for individual years is not recorded in the data table. Even if it were, year-to-year variability would obscure any trend as the fading data from most links is only generated from one or two years of observations. We can however make long-term observations of weather station data parameters that we find to be significant in predicting fading severity.

TABLE 1. Fading data records by region, showing coordinates, number of records, and number of different link locations, for each of the 20 regions. The mid-point coordinates of all links in each region are within 1500 km of the coordinates in the table.

Number	Latitude	Longitude	Fading Records	Locations	Region
1	+49.06	+1.12	48	42	Western Europe
2	+59.84	+21.11	42	28	Scandinavia
3	+53.01	+37.13	20	16	Russia
4	+42.31	+73.38	5	5	Central Asia
5	+45.12	–76.37	13	5	South-East Canada
6	+51.48	–122.1	10	9	South-West Canada
7	+74.78	–98.83	4	4	Arctic Canada
8	–25.27	–49.17	7	6	Brazil
9	+62.53	–65.72	4	4	North-East Canada
10	+24.85	+67.08	1	1	Pakistan
11	+30.84	+31.09	7	7	Egypt
12	+44.4	+10.95	79	55	Southern Europe
13	+5.76	+0.19	3	3	Ghana
14	+12.77	–16.11	3	2	Senegal
15	–16.54	+33.17	3	3	South-East Africa
16	–20.61	+132.9	50	15	Central-North Australia
17	–32.86	+142.1	91	31	South-East Australia
18	–25.59	+147.7	92	32	Southern Queensland
19	–30.62	+118.7	36	11	South-West Australia
20	–12.48	+142.3	17	7	Far North Queensland

The fading measurements used in this study date back to as early as 1953, with many of the measurements outside Australia occurring in the 1970's to 1990's. However, we use parameters generated from weather station data from 2010 to 2017. This is an appropriate time period for the Australian fading data, all from 2009 to the present, but is two or more decades later than the fading observed in other countries.

The possibility that there may have been some drift in the prediction parameters from weather stations, over time, must be considered. The 5626 stations for the years 2010 to 2017 includes many that are in regions where there was no fading data prior to 2007, so we exclude stations east of 90 degrees east longitude, or west of 140 degrees west longitude, or stations in the USA south of 40 degrees north latitude (there are no USA fading records in the data table, but a number of records from Canada). Only stations with continuous data for the years 2010 to 2017 as well as 1990 to 1997 are included in this comparison.

These leaves 616 stations where we compare parameters $N_{sA0.1}$ and $dN_{75\mathrm{mH}}$ from the years 2010 to 2017 with the same parameters from the same stations for years 1990 to 1997. For both these parameters, the number of stations having an increase or a decrease over the 20 years are reasonably similar; 55% of them have an increase in severity of $N_{sA0.1}$, while 46% of them have an increase in severity of $dN_{75\mathrm{mH}}$.

In the case of the $N_{sA0.1}$ parameter, the mean difference is -0.14 N-units, but an unweighted mean is an OLS estimate, which ignores spatial correlation that may exist between nearby stations. This correlation may be taken into account with a GLS estimate, using the methods described in [33], or later in this paper, as the mean difference is a regression model with only an intercept and no other parameters. In the case of $N_{sA0.1}$, the GLS estimate of the difference over 20 years is −0.40 N-units, but this is only marginally significant, with a 95% confidence interval from −0.84 to +0.04 N-units. While a time correction for $N_{sA0.1}$ drift does not appear essential, we assume the minor correction of −0.02 N-units per year, based on the GLS difference over 20 years.

The change in $dN_{75\mathrm{mH}}$ is less significant, with an OLS mean difference of +0.08 N-units, or a GLS estimated increase of 0.16 N-units. The 95% GLS confidence interval is from −0.27 to +0.58 N-units. Hence the 2010 to 2017 $dN_{75\mathrm{mH}}$ data appears appropriate for the earlier fading data.

The above results for $N_{sA0.1}$ and $dN_{75\mathrm{mH}}$, parameters significant for predicting clear-air fading, are in marked contrast to mean temperature difference for the same surface weather stations, comparing the same time periods. The overwhelming majority (95%) of these stations have 2010 to 2017 mean temperature greater than 1990 to 1997 mean temperature, with an OLS mean difference of +0.69 degrees. The GLS difference is +0.757 degrees, with a 95% confidence interval from +0.683 to +0.831 degrees.

III. WEATHER STATION DATA INTERPOLATION

A. ORDINARY KRIGING

Kriging in its various forms [36] is a popular technique for linear spatial interpolation as it is the Best Linear Unbiased Predictor (BLUP) if the assumptions relevant to the particular form of kriging are met. We therefore consider this as an option for interpolating our parameters from weather stations.

Named after D. G. Krige, who applied the idea to the prediction of the spatial distribution of ore content, kriging was fully described later [37]. Ordinary kriging is the most popular form of this technique, and assumes the data has a stationary but unknown mean, and has stationary and known isotropic spatial variation, as a function of distance. The ordinary kriging system can be described as

$$\begin{bmatrix} w_1 \\ \vdots \\ w_n \\ \mu \end{bmatrix} = \begin{bmatrix} \gamma_{1,1} & \cdots & \gamma_{1,n} & 1 \\ \vdots & \ddots & \vdots & \vdots \\ \gamma_{n,1} & \cdots & \gamma_{n,n} & 1 \\ 1 & \cdots & 1 & 0 \end{bmatrix}^{-1} \begin{bmatrix} \gamma_{1,P} \\ \vdots \\ \gamma_{n,P} \\ 1 \end{bmatrix} \tag{21}$$

where $w_1..w_n$ are the weights applied to the n data points, the terms $\gamma_{i,j}$ are the predicted semivariogram function $\gamma(h)$ values for the distances between pairs of known points i and j, and $\gamma_{i,P}$ are the predicted $\gamma(h)$ values for the distances $h(i, P)$ between known points and the interpolation point.

A number of different semivariogram functions $\gamma(h)$ may be used [38], and the *nugget effect* is often employed, where $\gamma(h)$ is discontinuous at the origin, with $\gamma(h = 0) = 0$ and $\gamma(h > 0) > 0$. This allows the fitted surface to not pass through the known points. However, we are considering exact interpolation, so the semivariogram functions described below are continuous, forcing the interpolated surface to pass through the known points. We find this to be workable provided the semivariogram function has non-zero, and preferably maximum, slope at the origin.

Two useful functions for map interpolation are the exponential function

$$\gamma(h) = \sigma^2[1 - \exp(-h/h_0)], \tag{22}$$

and the power function

$$\gamma(h) = b|h|^{\lambda}, \quad 0 \leq \lambda < 2. \tag{23}$$

In (22), σ^2 is the data variance, although the weights given by (21) are independent of the value of σ^2, or the value of constant b in (23). Therefore, we may fit the semivariogram function to the data by varying one constant, h_0 in (22), or λ in (23), to find the minimum RMS interpolation error, as indicated by cross-validation.

Alternatively, (21) may have covariance terms, for example $C_{i,j} = \sigma^2 \exp(-h(i,j)/h_0)]$ in the case of the exponential function, replacing the $\gamma_{i,j}$ terms. This is an equivalent formulation, except the Lagrange parameter μ then has the opposite sign. The $n+1$'th row and column in the semivariogram or covariance matrix provides unity sum of weights, ensuring a fit to the unknown mean of the data.

The stationary mean and covariance assumption of ordinary kriging is unlikely to be met with world-wide surface weather station data, with widely varying terrain and climate types, so kriging may not necessarily be the BLUP.

Another problem for our application is that (21) requires inversion of an $n+1$ by $n+1$ matrix, readily achieved if n is a few hundred or less, but we are interpolating data from several thousand weather stations world-wide. A solution to this problem may be expected to be to restrict the kriging to a smaller number of local points, but we find that that introduces discontinuities in the interpolated surface.

B. NATURAL NEIGHBOUR INTERPOLATION

Natural neighbour interpolation provides a unique exact interpolation that guarantees continuous first and second derivatives everywhere except at the known points [39], while only depending on local data, the natural neighbours of the interpolation point. Voronoi polygons contain all locations that are closer to a particular data point location than any other, and natural neighbours are data points with adjoining Voronoi polygons.

Conceptually, natural neighbour interpolation is very simple, as illustrated in Fig. 2. If the interpolation point is treated as a new data point, then the weights assigned to its natural neighbours are proportional to the overlap areas of its Voronoi polygon (red dashed line) with the previously existing Voronoi polygons.

Natural neighbour interpolation is well suited to our problem of interpolating over the surface of the Earth, as this surface has no boundary, requiring special treatment. If we assume the Earth to be spherical, then spherical polygon areas are easily calculated from the sum of internal angles [40]. Natural neighbour interpolation is ideally suited to interpolation of parameters from highly irregular distributed locations [39], as is the case with our weather stations. This interpolation method appears to have the ability

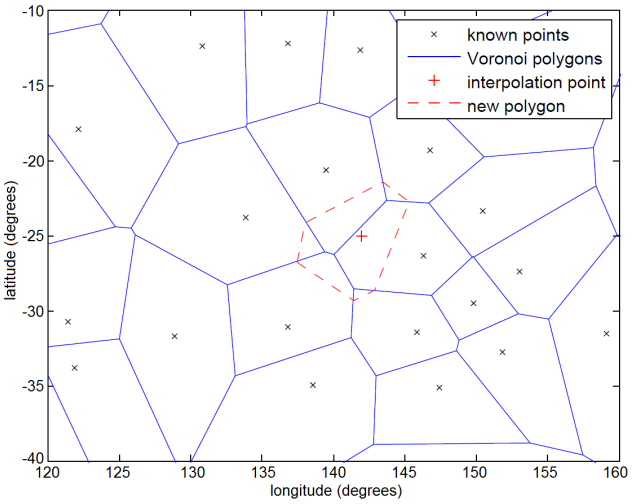

FIGURE 2. Natural neighbour interpolation: an example showing the Voronoi polygons corresponding to the known points, overlapped by a new polygon for a location to be interpolated. The interpolation weights are proportional to the six areas of overlap of the original polygons.

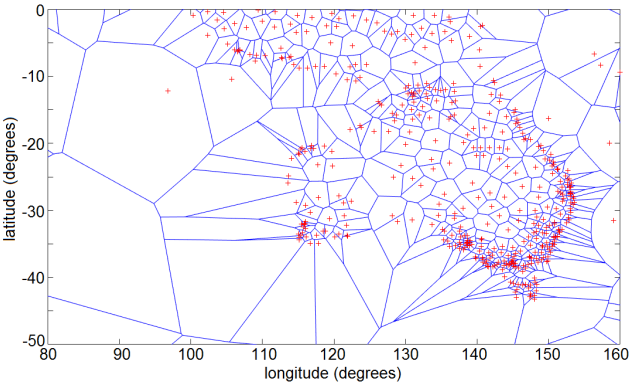

FIGURE 3. Voronoi polygons for surface weather stations in the Australian region. The red crosses are station locations, and those on the west coast of Australia have polygons extending far into the Indian Ocean, where there are few stations. Coastal stations a little further to the west than their neighbours appear to have disproportionally large Voronoi polygons.

to generate an interpolated surface from only the neighbours of the interpolation point, to rival that achieved by kriging using all known points, in terms of smoothness and accuracy. We compare accuracies, by cross-validation, below. Using only local data is an advantage, as it obviates any stationarity requirement.

However, points far removed from the interpolation point may be given considerable weight if the data points are very irregularly spaced [41], as is the case with surface weather station data. This is likely to be the case for coastal weather stations having large Voronoi polygons extending out into the ocean where there are few stations. Fig. 3 demonstrates this for the Australian region.

We introduce an amendment to combat the irregular polygons displayed in Fig. 3. Each vertex of a Voronoi polygon is the centre of a circumcircle of three or more data point locations. The radii of the circumcircles of the vertices of

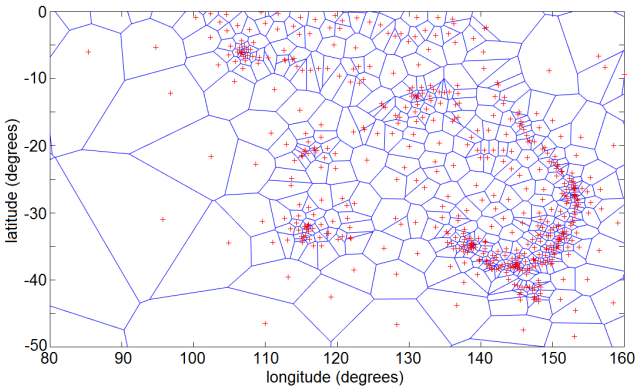

FIGURE 4. Voronoi polygons for surface weather stations in the Australian region, with additional interpolated "quasi-stations" to eliminate very irregular polygons. These interpolated points are added at polygon vertices until no polygon has vertex circumcircle radii spanning a ratio exceeding 5:1.

a polygon will vary greatly in the case of polygons with a centroid far removed from the corresponding data point.

A potential solution to the problem may be to identify the polygon with the largest ratio between maximum and minimum radius of its vertex circumcircles. If that ratio exceeds a pre-defined threshold, say 5:1, then the natural neighbour interpolated value at the maximum radius vertex of that polygon is calculated, and a new ''quasi-known'' point is created at that location. That process is repeated until no polygons have a maximum to minimum vertex circumcircle ratio exceeding the threshold value. The result of that process applied to the stations of Fig. 3 is shown in Fig. 4, for a radius ratio threshold of 5:1.

C. INTERPOLATION TESTING

The Harvey [14] 75 m subrefractive parameter $dN_{75\mathrm{mH}}$ in the Australian region is a sensitive test case for different interpolation methods, as it varies over a wide range over much of the Australian land mass, more extensively than any other continent. The results of interpolation testing for 354 weather stations in this region (latitudes 10 to 50 degrees south, longitudes 90 to 160 east), by leave-one-out cross-validation are shown in Table 2.

We test ordinary kriging (OK) with the lowest RMS error exponential model and power model found in the testing, as well as conventional natural neighbour interpolation (NNI, no infill), and added interpolated points as described above (NNI, infill if ratio>5:1).

A popular ad-hoc interpolation method in the past was Shepard interpolation [42]. It is often rather incorrectly described as inverse distance weighting, but in fact the algorithm is far more involved than that. A good detailed description of the algorithm is given in [43]. The interpolation uses a small number of closest local known points, typically 7, but always at least 4 in sparsely populated regions and no more than 10 in heavily populated regions. We use the point

TABLE 2. Leave-one-out interpolation cross-validation for parameter $dN_{75\mathrm{mH}}$ from 354 weather stations in the Australian region. Ordinary kriging (OK) with a power model has lowest RMS error, closely followed by the exponential model and natural neighbour interpolation (NNI) with added points.

Method	details	RMS error	correl. coeff. R
OK, 50 closest	exponential, $h_0 = 1500$	7.5558	0.83899
OK, 50 closest	power, $\lambda = 0.7$	7.5038	0.84009
NNI	original, no infill	7.7117	0.83164
NNI	infill if ratio>5:1	7.5638	0.83766
Shepard	complete algorithm	7.8970	0.82220

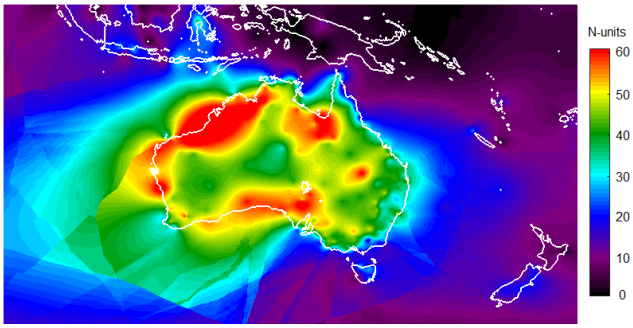

FIGURE 5. Ordinary kriging of $dN_{75\mathrm{mH}}$ from the 50 closest stations, with a power model $\gamma(h) = b|h|^{0.7}$, for the Australian region. Leakage of high overland values to the ocean to the south-west is seen, and discontinuity where high-value stations are included or excluded from the kriging system.

selection method and complete interpolation algorithm as described in [43], for the Shepard results in Table 2.

For each method, leave-one-out testing is used; for each station the observed value is compared with an interpolation that does not include that station. The RMS error (N-units), and Pearson's correlation coefficient, R, between the observed and interpolated values, are shown in Table 2.

Although ordinary kriging with a power model, $\gamma(h) = b|h|^{0.7}$, has lowest RMS error and best correlation in Table 2, this method, using the 50 closest points, is less local than natural neighbour interpolation, using typically 6 natural neighbours. As a result, the kriging interpolation appears to suffer more than NNI from leakage of the high coastal and inland values into the ocean where values are low but measurements very sparse. In addition, kriging with just the 50 closest stations suffers from discontinuities as outlier stations are switched in or out of the interpolation. These effects are demonstrated for kriging in Fig. 5.

Fig. 6 shows the same parameter, with natural neighbour interpolation, modified by adding interpolated points to eliminate vertex circumcircle radius ratios exceeding 5:1. While this seems to improve accuracy, judging by the results in Table 2, conventional natural neighbour interpolation, shown in Fig. 7, has smoother contours and appears to have less leakage of land values into the ocean than the modified method of Fig. 6.

The added points in the modified method of Fig. 6 potentially add discontinuities in the derivatives of the interpolated

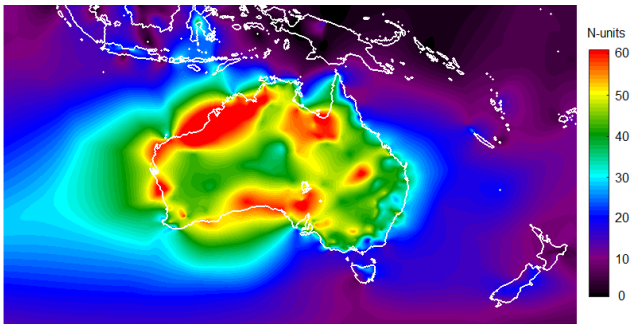

FIGURE 6. Natural neighbour interpolation, with added points to eliminate vertex circumcircle radius ratios exceeding 5:1, of parameter $dN_{75\mathrm{mH}}$. While leave-one-out testing suggests these added points improve accuracy, the contours in ocean areas appear to be less smooth than the conventional technique, and leakage of land values into ocean areas may be increased.

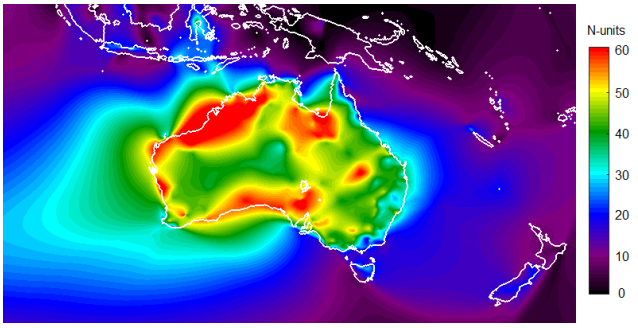

FIGURE 7. Conventional natural neighbour interpolation of weather station parameter $dN_{75\mathrm{mH}}$. A smooth interpolated surface is obtained even though only a small number of local points are used in each interpolation.

surface. This may be the reason for the Indian ocean contours in Fig. 7 being smoother than those in Fig. 6.

Accordingly, we choose conventional natural neighbour interpolation to produce digital maps of the weather station parameters, as cross-validation indicates it is close to the accuracy achieved by kriging, while producing a superior digital map.

In practice a digital map on a regular grid, at a spacing typically in the region of 0.5 degrees in latitude and longitude, is used to obtain parameter values for radio link design. The path center coordinates of the link are used to interpolate a value. Two methods of doing this are provided in [44]. Bilinear interpolation from the four grid points surrounding the interpolation location has been generally used, but bicubic interpolation may be considered. We test these options by producing the world-wide digital map from the station data, on a 0.5 degree grid, using natural neighbour interpolation, and then re-interpolate back from the grid to the station coordinates, and observe the error.

The unexpected result is that bilinear interpolation appears to be generally more accurate than bicubic interpolation, when tested in this way, so in the following regression models, we use bilinear interpolation of values from a digital map with a 0.25 degree grid spacing. This replicates the procedure to be used by link designers in making a prediction, rather than interpolating directly from weather station locations to link locations.

IV. DEVELOPMENT OF THE NEW MODEL

A. OLS AND GLS

A detailed desciption of OLS and GLS estimation is given in [33], but briefly, OLS assumes uncorrelated errors, and the regression coefficients $\mathbf{b}_{\mathrm{OLS}}$ are given by

$$\mathbf{b}_{\mathrm{OLS}} = (\mathbf{X}'\,\mathbf{X})^{-1}\mathbf{X}'\mathbf{y}, \tag{24}$$

where $\mathbf{y}$ is the column vector of observed responses, corresponding to the rows of matrix $\mathbf{X}$, whose columns are the prediction parameters, the first column being all ones, to estimate the intercept, the first element of $\mathbf{b}_{\mathrm{OLS}}$. The regression model estimate $\hat{\mathbf{y}} = \mathbf{X}\mathbf{b}_{\mathrm{OLS}}$ minimises the sum of squared residuals $\mathbf{e} = \hat{\mathbf{y}} - \mathbf{y}$.

If the errors are known to be correlated, GLS estimation minimises the squared residuals of a transformed problem, the aim being to eliminate error correlation by pre-multiplying $\mathbf{X}$ and $\mathbf{y}$ by symmetrical matrix $\mathbf{P}$:

$$\mathbf{b}_{\mathrm{GLS}} = (\mathbf{X}'\mathbf{S}^{-1}\,\mathbf{X})^{-1}\mathbf{X}'\mathbf{S}^{-1}\mathbf{y}$$

where

$$\mathbf{S}^{-1} = \mathbf{P}'\mathbf{P}. \tag{25}$$

For simplicity, we assume an exponential spatial correlation function [33] of the form

$$\phi_{ij} = (1 - k_n)\exp\left(-\frac{r_{ij}}{r_0}\right), \tag{26}$$

where r_{ij} is the distance between different locations i and j, to give matrix $\mathbf{S}$ as

$$\mathbf{S} = \begin{pmatrix} 1 & \phi_{12} & \phi_{13} & \cdots & \phi_{1n} \\ \phi_{21} & 1 & \phi_{23} & \cdots & \phi_{2n} \\ \phi_{31} & \phi_{32} & 1 & \cdots & \phi_{3n} \\ \vdots & \vdots & \vdots & \ddots & \vdots \\ \phi_{n1} & \phi_{n2} & \phi_{n3} & \cdots & 1 \end{pmatrix}. \tag{27}$$

The suitability of the GLS scheme may be judged by a correlation test on the transformed residuals $\mathbf{Pe}$. We do this with a spatial equivalent [33] of the Durbin-Watson statistic d_w, the sum of squared residual forward differences divided by the sum of squared residuals. A value of d_w close to 2 is expected for uncorrelated residuals; $d_w < 2$ for a positive correlation, or $d_w > 2$ for a negative correlation.

The parameters in (26) are found by producing a semivariogram $\gamma(h)$ of the OLS residuals, using the Cressie-Hawkins robust estimator [38] applied to distance classes numerically equal to the number of residual pairs with zero geographic distance ($h = 0$). The sill value of the semivariogram is assumed to be OLS residual variance σ_{OLS}, and the nugget parameter k_n is set to the Cressie-Hawkins estimate of $\gamma(h = 0)$ divided by σ_{OLS}. The parameter r_0 is set to the value where equal numbers of the semivariogram estimates for distances

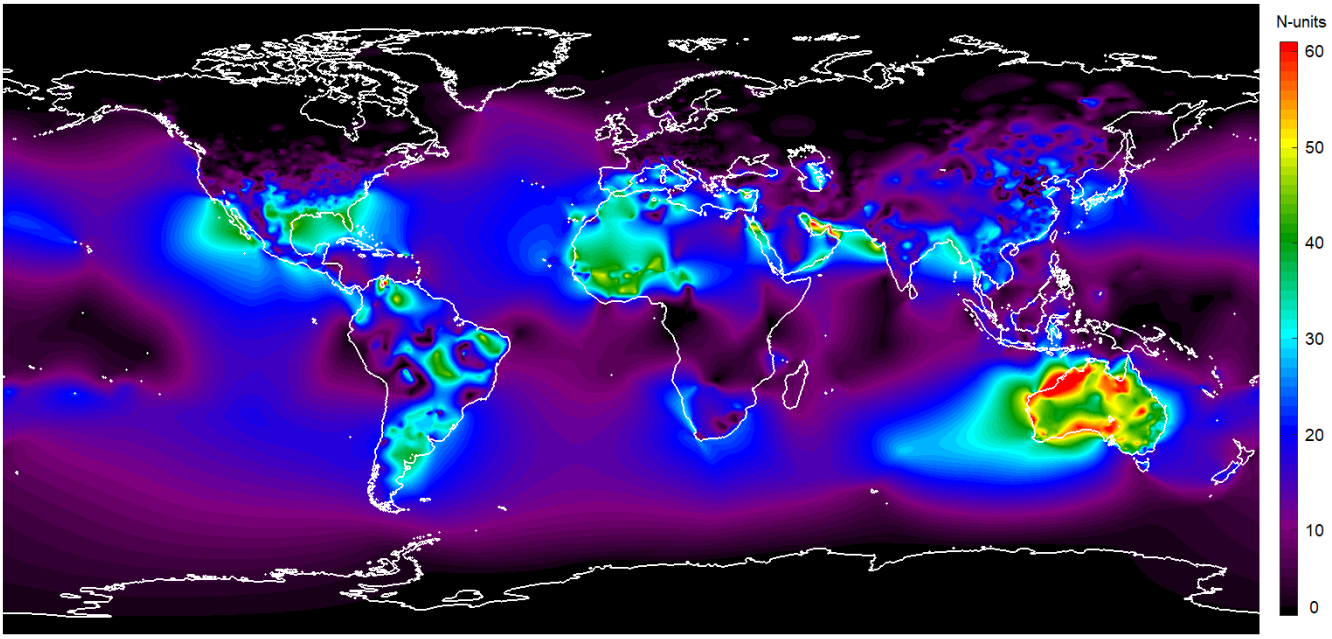

FIGURE 8. Worldwide map of the Harvey model for worst-case radio refractivity increase with height in the lowest 75 m of the atmosphere, $dN_{75\mathrm{mH}}$.

less than 2000 km are above and below the exponential curve $\gamma(h) = \sigma_{\mathrm{OLS}}[1 - (1 - k_n)\exp(-h/r_0)]$.

While OLS estimation of the regression parameters minimises the RMS error of the model with respect to observations included in the model fitting, we explore the use of GLS regression models, the aim being to reduce the influence of spatially correlated observations. The effective spatial Durbin-Watson statistic [33] of the residuals of the following OLS model, $d_w = 1.06$, indicates very significant positive spatial correlation. The GLS model, with $k_n = 0.105$ and $r_0 = 219.5$ km, has transformed residual $d_w = 1.95$, indicating substantial elimination of the spatial correlation.

B. CROSS-VALIDATION AND PARAMETER SELECTION

In previous OLS regression models for multipath fading [26], [32], model parameters have been selected one at a time, as the one with the strongest correlation, initially with the observations, and then with the residuals of the previous regression model. The risk with this procedure is that an initially significant parameter may become insignificant, as more parameters are added.

Another problem is that if OLS residual RMS is taken as the criterion, without cross-validation (testing with observations not included in the model fitting), the model will appear to always improve as new parameters are added, whether they are really useful or not.

We address these problems by a form of cross-validation that may be described as *leave-one-region-out*. For each of the regions described in Table 1, predictions are performed with regression models fitted to the data from the other 19 regions. Rather than progressively adding parameters to the model, all possible binary combinations of including or not including parameters in the model are tested, and the combination producing the lowest overall leave-one-region-out RMS error is chosen.

The parameters are similar to those in (20), but using more extensive weather station data, and with some improvements, as follows.

A new parameter H_{8500} is now included, the mean rayline clearance (m) above terrain (ignoring tree cover, as its height is often unknown) at standard refractivity gradient (effective Earth radius of 8500 km).

The subrefractive parameter v_2 of (19) is now replaced by v_{sr}, now depending on path length d (km) as well as H_{8500}, to avoid excessive values for low clearance very short paths in regions of high $dN_{75\mathrm{mH}}$:

$$v_{\mathrm{sr}} = \left(\frac{dN_{75\mathrm{mH}}}{50}\right)^3 \exp\left(-\frac{H_{8500}}{4\sqrt{d}}\right). \tag{28}$$

The cubic dependency with $dN_{75\mathrm{mH}}$ is retained, as that is found to provide better accuracy than alternative exponents.

A world-wide map of $dN_{75\mathrm{mH}}$ is shown in Fig. 8. This parameter suggests that subrefraction appears to be a wide-spread and severe problem in much of Australia, more so than other countries. West Africa and parts of the Americas in particular, appear to have subrefraction of lesser severity.

After testing of a number of different options, we find that a new path inclination parameter $|\epsilon_p|^{0.2}$ appears to be an improvement over the conventional $\log(1 + |\epsilon_p|)$.

The recent inclusion of a number of relatively low frequency 2 GHz records in the fading data, reduces uncertainty in estimating frequency dependence of the model. A new frequency parameter $\log(f^2 + 36)$ appears to be more significant

TABLE 3. Best leave-one-region-out cross-validated OLS (RMS error 5.94 dB) and GLS (RMS error 5.96 dB) models. Both regression coefficients, and the corresponding *t*-statistics, indicating statistical significance, are shown. As there are many data points, the *t*-distribution here is close to a normal distribution with unit variance.

Parameter	OLS coefficient	OLS *t*-statistic	GLS coefficient	GLS *t*-statistic
(Intercept)	–43.2	–8.94	–39.65	–7.47
$\log(d)$	+35.18	+22.3	+34.21	+19.5
$\log(f^2+36)$	+8.728	+6.67	+5.761	+5.35
$\lvert\epsilon_p\rvert^{0.2}$	–9.679	–9.35	–7.284	–6.98
h_L	–0.00564	–5.72	–0.00167	–1.31
$\tanh((H_{8500}-250)/75)$	–2.247	–4.06	–2.805	–4.39
$v_{\rm sr}$ (28)	+36.18	+7.19	+48.06	+6.79
$\tanh((S_a-70)/50)$	–2.564	–5.26	–3.217	–3.47
dN_1	–0.01261	–4.82	–0.01089	–1.92
$N_{sA0.1}$	–0.1878	–8.97	–0.1655	–3.07

than the previous parameters $\log(f+6)$ in (20), or $\log(f)$ in the current ITU-R model [12].

Terrain area standard deviation S_a is used in this new model, similar to that employed in [12], but with a refined method of evaluation.

The new S_a is a standard deviation from the same 30 second terrain data, but over a circular area of 100 km radius, with raised cosine weighting tapering to zero at the edge of the area. In order to avoid undue weighting of polar regions due to the longitude grid converging at the poles, random sampling of the terrain data with probability $4\cos(\phi)$, where ϕ is latitude in radians, is used at latitudes with magnitude exceeding 75.522 degrees.

The regression coefficients for the best OLS and GLS models, found by leave-one-region-out cross validation, are shown in Table 3. The best OLS and GLS models each have the same 9 parameters.

There are some minor differences in the regression model coefficients between the OLS and GLS models, and their significance indicated by the t-statistic is generally less for the GLS model than the OLS model.

The most extreme example of this coefficient difference is the elevation of the lowest antenna, h_L. It has a coefficient of -0.00564 dB per m in the OLS model, and highly significant with $t = -5.72$. In the GLS model its coefficient is -0.00167 dB per m, and barely significant with $t = -1.31$. However, we retain it in the GLS model as the leave-one-region-out cross-validation suggests that it is useful.

The new GLS model

$$\begin{aligned} A_{0.01} = {} & -39.65 + 34.21\log(d) - 7.284|\epsilon_p|^{0.2} \\ & - 3.217\tanh((S_a-70)/50) + 5.761\log(f^2+36) \\ & - 0.01089dN_1 - 0.00167h_L \\ & - 2.805\tanh((H_{8500}-250)/75) \\ & + 48.06v_{\rm sr} - 0.1655N_{sA0.1}\ \text{dB} \end{aligned} \tag{29}$$

has parameters $\log(d)$, h_L and dN_1 in common with the current ITU-R model [12] for detailed design

$$\begin{aligned} A_{0.01} = {} & -44 + 34\log(d) - 10.3\log(1+|\epsilon_p|) \\ & - 4.6\log(10+s_a) + 8\log(f) \\ & - 0.027dN_1 - 0.0076h_L\ \text{dB}, \end{aligned} \tag{30}$$

while (29) has revised forms of the frequency f, path inclination ϵ_p and terrain area standard deviation S_a parameters, as well as a new subrefractive parameter $v_{\rm sr}$, path clearance parameter $\tanh((H_{8500}-250)/75)$, and surface refractivity anomaly parameter $N_{sA0.1}$.

TABLE 4. Mean and standard deviation of prediction error by region, showing number of records, error statistics of the existing Rec. ITU-R P.530 model, and the new GLS model of Table 3. Significant mean under-prediction by the P.530 model in Central Asia, Ghana, and Northern Australia, is largely eliminated by the new GLS model, and is substantially reduced in Arctic Canada.

Records	P.530 mean	P.530 std dev	GLS mean	GLS std dev	Region
48	–0.96	4.94	–2.29	4.83	Western Europe
42	–0.37	5.48	–3.50	5.08	Scandinavia
20	+2.87	4.82	+0.51	4.28	Russia
5	–5.86	9.76	–0.02	7.21	Central Asia
13	+2.95	4.94	+1.71	5.43	South-East Canada
10	+5.75	4.93	+7.80	2.77	South-West Canada
4	–11.2	10.0	–7.01	9.54	Arctic Canada
7	+0.17	6.25	+2.34	4.50	Brazil
4	–1.38	6.27	+1.79	6.16	North-East Canada
1	+2.14	—	+2.10	—	Pakistan
7	–0.55	7.76	–5.86	6.64	Egypt
79	–0.49	6.13	–1.51	5.63	Southern Europe
3	–9.34	4.21	–2.29	3.61	Ghana
3	–1.47	5.87	–3.90	2.16	Senegal
3	+1.08	3.52	+3.42	2.95	South-East Africa
50	–9.83	7.27	–0.54	6.44	Cent-North Australia
91	–3.69	5.71	+0.77	5.32	South-East Australia
92	–6.02	6.52	–1.36	4.84	Southern Queensland
36	+0.57	5.60	+4.91	4.41	South-West Australia
17	–6.09	5.18	–2.12	5.11	Far North Queensland
535	–2.84	6.99	–0.49	5.72	All Regions

C. ACCURACY OF THE NEW GLS MODEL

The prediction error statistics of the GLS model of Table 3 are detailed in Table 4, separated into the 20 regions of Table 1, as well as overall. The error statistics for predictions with the current ITU-R model [12] are shown for comparison. The new GLS model demonstrates a significant improvement in accuracy over the ITU-R model in Central Asia, Ghana, and the three northern Australian regions, due to elimination of the large mean underprediction errors of the ITU-R model in these regions.

Overall, the new GLS model has less less mean error and lower error standard deviation than the current ITU-R model. Next we consider the alternative approach of treating multipath fading and subrefractive median depression fading as separate mechanisms.

D. COMPARISON WITH SEPARATE MULTIPATH AND LINEAR SUBREFRACTIVE GRADIENT MODELS

A conventional approach [14], [15] assumes a linear refractivity gradient diffraction loss model for subrefractive median depressions, with a separate multipath model to represent other clear-air fading events. We simulate this approach by taking the GLS model of Table 3 or (29), omitting the subre-

fractive term +48.06 v_{sr}, as the non-subrefractive multipath model for fade depth $A_{0.01MP}$ for 0.01% of the worst month of the average year. The subrefractive model for fade depth for 0.01% of the worst month $A_{0.01SR}$ is estimated as 10 dB greater than the diffraction loss estimated for a worst-case subrefractive gradient, assumed to represent the gradient for 0.1% of the worst month. The diffraction loss is predicted using the "method for a general terrestrial path" of [45]. The added 10 dB accounts for Rayleigh fading, assumed to be present during the subrefractive fade. The predicted fade depths for the two mechanisms are then combined as

$$A_{0.01} = 10 \log \left[10^{\frac{A_{0.01MP}}{10}} + 10^{\frac{A_{0.01SR}}{10}} \right]. \quad (31)$$

Path profiles, of terrain elevation with distance along the path, are available for 483 of the 535 data records in this study, so we compare our GLS model with the above linear subrefractive gradient approach for these records. For these the GLS model has a mean error of −0.41 dB, and an error standard deviation of 5.72 dB. The parameters for the Schiavone subrefractive model [15] are not available for the fading data locations, so we test two models based on the Harvey model for worst-case gradient at a location, dN_{75mH}.

1) ORIGINAL HARVEY EFFECTIVE GRADIENT MODEL

A model for an effective uniform linear refractivity gradient G_H along a path [14] was estimated from the model for effective Earth radius factor K_{e39} for a 39 km path:

$$K_{e39} = \frac{0.6}{1 + \frac{dN_{75mH}}{11.775}} + 0.17. \quad (32)$$

This is scaled in proportion to the square root of path length d, to give the Harvey effective gradient G_H as

$$G_H = 157 \left[\frac{1}{K_{e39}} \sqrt{\frac{39}{d}} - 1 \right] \quad \text{N-units per km.} \quad (33)$$

This model was based on measurements at locations with very severe subrefractive fading, but tends to be too severe at many locations. For the 483 test paths the mean error of (31) with this gradient model is +24.4 dB, with error standard deviation of 31.1 dB; significantly inferior to the GLS result.

2) COMBINED HARVEY-BOITHIAS-BATTESTI GRADIENT MODEL

We suggest an alternative subrefractive gradient model, based on (15), a model for a "continental temperate" climate. There is no indication in [11] of the actual location of the radio links used to develop this model, but the mean value of dN_{75mH} for the 222 weather stations in France, Spain, Switzerland, and Liechtenstein in our data, is 11.01 N-units. Assuming then that "continental temperate" climate corresponds to $dN_{75mH} = 11$, and scaling according to dN_{75mH}, we have the effective subrefractive gradient model

$$G_{HBB} = \frac{dN_{75mH}}{11} \left[\frac{2670}{d} - 13 \right] \quad \text{N-units per km.} \quad (34)$$

This model performs well for the 483 records where path profiles are available: mean error of (31) with this gradient model is +0.001 dB, with error standard deviation of 5.93 dB. This is close to the accuracy of the GLS model, so we compare this subrefractive plus multipath model (31) with the GLS model for its accuracy in predicting fading severity variation with antenna height (height gain).

E. HEIGHT-GAIN PREDICTION

An important issue for the guidance of radio link designers is accurate prediction of improvement with antenna height, for systems severely affected by median depression fading. If this fading is attributed to subrefaction, assuming a linear refractivity gradient model, a considerable improvement with antenna height may be predicted, so we compare the height-gain predictions with this type of model with the predictions from our Table 3 GLS model.

There are a number of records in the fading data with simultaneous observations at two different receive antenna heights, where the data was collected from space-diversity systems. We identify those likely to have significant subrefractive fading as those where the contribution to the GLS model from parameter v_{sr} at both antennas exceeds 3 dB. This yields 38 pairs of measurements, all from Australia.

The mean error of the GLS model for these 76 observations is −0.93 dB with 5.89 dB standard deviation. For these same observations, the linear gradient subrefractive model of (31) and (34) predicts $A_{0.01}$ with a mean error of −0.40 dB with 6.35 dB standard deviation.

The real interest is the prediction of fade depth reduction with antenna height, or height gain. In this respect, the GLS model performs well, with a mean prediction error of −0.26 dB, and 2.59 dB standard deviation. The subrefractive gradient diffraction model has mean +0.92 dB over-prediction of height gain, with 2.86 dB standard deviation. The mean of the latter appears small, but is not much less than the mean observed height gain of +1.47 dB.

The GLS model predicts 65.8% of the height gains within 2 dB of observed value, while the subrefractive model of (31) and (34) only predicts 34.2% of the height gains within 2 dB, and in fact over-predicts 44.7% of them by more than 2 dB.

F. CLEARANCE CRITERIA

The conventional approach to line-of-sight radio links [12] requires grazing line-of-sight clearance at the refractivity gradient given by (15) in a temperate climate, or an unobstructed path at this gradient in a tropical climate. An alternative proposal [16] is to design for a limited amount of obstruction fading, estimated by assuming diffraction loss at a certain positive refractivity gradient. The height-gain results described above suggest that the new GLS model we propose may be a more reliable basis for this type of approach than diffraction loss estimates assuming a linear refractivity gradient, due to the greater height-gain accuracy of the GLS model.

Often radio links employ various diversity reception schemes [11], [12] to improve performance, by taking advantage of multiple receivers with partially correlated fading. This breaks down if the depth of median depression fade approaches or exceeds the system fade margin. Amendments to diversity improvement prediction models in the most recent version of the ITU-R Recommendation [12], now ensure that fading severity is now taken into account for all forms of diversity reception.

Thus it may be feasible to replace clearance criteria for choosing antenna heights, by performance predictions using the new GLS model, subject to validity of that model. As an empirical model, the GLS model may be considered valid for the range of parameters represented in the data.

We find no evidence that the accuracy of the model is affected for median refractivity path clearances approaching grazing line-of-sight, despite several dB of predicted path obstruction. We note here that the GLS model is for fading with respect to median signal level, not unobstructed free-space signal level. There is just one case, the fading of a space diversity receiver in a 1.8 GHz system, where grazing line-of-sight clearance is not quite achieved at median refractivity gradient, yet the error in the GLS fading prediction error is only 3.4 dB overprediction.

Considering these results, we suggest that provided the design meets availability and performance specifications, using the new GLS multipath model together with the recently revised diversity improvement models of [12], the clearance criteria of [12] may be relaxed, by applying them at median refractivity gradient (nominally -39 N-units per km), instead of the currently suggested subrefractive gradient of (15). This may lead to more economical system designs in some cases.

V. UNIVERSAL KRIGING

Universal kriging [36] extends ordinary kriging of (21) to allow for non-stationary mean, estimated in terms of p functions of location s, $f_1(s)$ to $f_p(s)$. The semivariogram matrix $\mathbf{G}$ is similar to that in (21), but with additional rows and columns for the functions $f_1(s)$ to $f_p(s)$:

$$\mathbf{G} = \begin{bmatrix} \gamma_{1,1} & . & \gamma_{1,n} & 1 & f_1(s_1) & . & f_p(s_1) \\ . & . & . & . & . & . & . \\ \gamma_{n,1} & . & \gamma_{n,n} & 1 & f_1(s_n) & . & f_p(s_n) \\ 1 & . & 1 & 0 & 0 & . & 0 \\ f_1(s_1) & . & f_1(s_n) & 0 & 0 & . & 0 \\ & . & . & . & . & . & . \\ f_p(s_1) & . & f_p(s_n) & 0 & 0 & . & 0 \end{bmatrix} \tag{35}$$

and the value at location s_P is obtained as a weighted mean of the n known values at locations s_1 to s_n. The weights w_1 to w_n are given by

$$\begin{bmatrix} w_1 \\ \vdots \\ w_n \\ m_0 \\ m_1 \\ . \\ m_p \end{bmatrix} = \mathbf{G}^{-1} \begin{bmatrix} \gamma_{1,P} \\ \vdots \\ \gamma_{n,P} \\ 1 \\ f_1(s_P) \\ . \\ f_n(s_P) \end{bmatrix}. \tag{36}$$

If a semivariogram function without nugget effect is used, such as (22) or (23), the result of (36) is a smooth interpolation surface that passes through the known points, and close to them it is predominantly interpolated from them. If the nugget effect is employed, as in (26), the requirement to pass through the known points is relaxed, and in their region the surface is a best fit rather than an exact interpolation. We use the same exponential model with nugget effect, (26), that we use for the GLS estimation. As a semvariogram function, (22) then becomes

$$\gamma(r_{ij}) = \sigma^2[1 - (1 - k_n)\exp(-r_{ij}/r_0)] \quad \text{for } i \neq j,$$

otherwise

$$\gamma(r_{ij}) = \sigma^2. \tag{37}$$

At locations distant from known points the estimation becomes predominantly a GLS estimate in terms of the functions $f_1(s)$ to $f_p(s)$.

A. APPLICATION TO FADING PREDICTION

Geoclimatic factor may defined for a multipath fading model as the part of the model that is invariant for any link with the same path center coordinates. For the GLS model of Table 3, it may be defined as

$$\begin{aligned} K_G = {} & -39.65 - 3.217\tanh((S_a - 70)/50) \\ & - 0.01089dN_1 - 0.1655\log(N_{sA0.1})\ \text{dB}. \end{aligned} \tag{38}$$

The predicted fade depth for 0.01% of the worst month $A_{0.01}$ is then

$$\begin{aligned} A_{0.01} = {} & K_G + 34.21\log(d) + 5.761\log(f^2 + 36) \\ & - 7.284|\epsilon_p|^{0.2} - 0.00167h_L + 48.06v_{\text{sr}} \\ & - 2.805\tanh((H_{8500} - 250)/75)\quad \text{dB}. \end{aligned} \tag{39}$$

The subrefractive parameter v_{sr} is included in (39), and not in the geoclimatic factor (38), because its value, given by (28), depends on mean rayline clearance height H_{8500} and path length d, as well as the Harvey subrefractive climate parameter $dN_{75\text{mH}}$.

At locations where link fading data provides an observed value of $A_{0.01}$, an observed value of K_G may be obtained by re-arranging (39) as

$$\begin{aligned} K_G = {} & A_{0.01} - 34.21\log(d) - 5.761\log(f^2 + 36) \\ & + 7.284|\epsilon_p|^{0.2} + 0.00167h_L - 48.06v_{\text{sr}} \\ & + 2.805\tanh((H_{8500} - 250)/75)\ \text{dB}. \end{aligned} \tag{40}$$

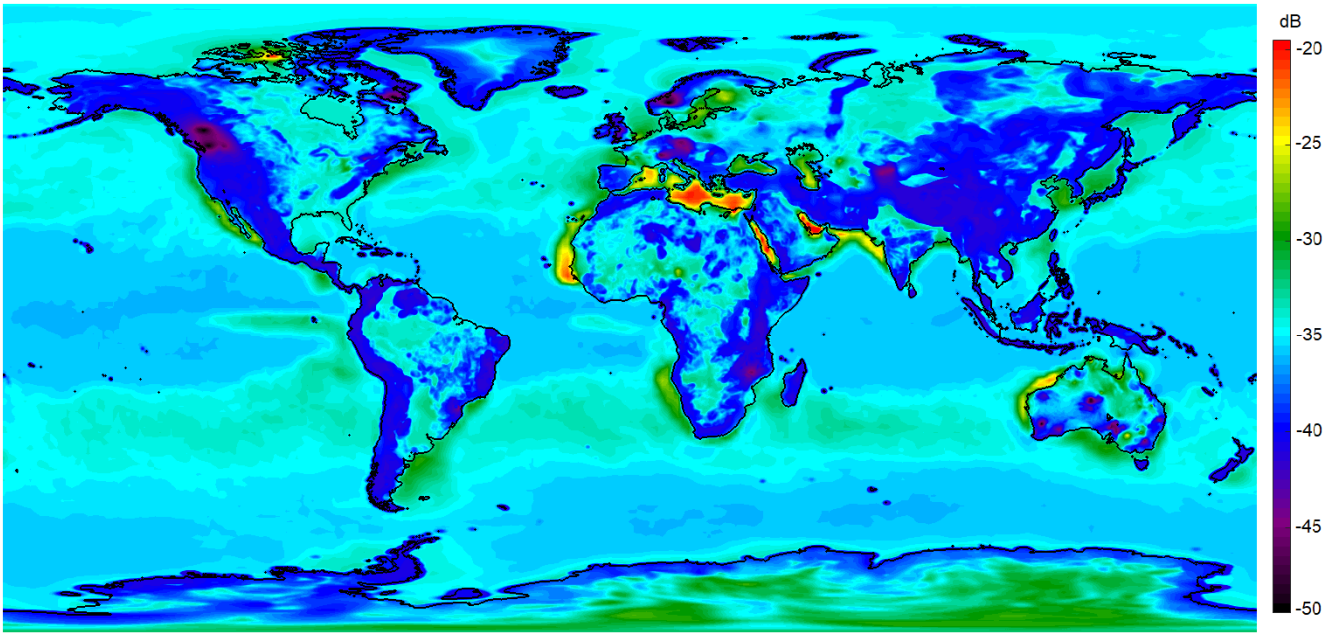

FIGURE 9. Worldwide map of geoclimatic factor K_G, produced by universal kriging. This indicates predicted severity of multipath fading.

If there is more than one observation at the same location, we take the mean of the K_G values for those observations.

The universal kriging system of (35) and (36) is set up, using the exponential semivariogram function (37), and the functions f_1 to f_p are the parameters $\tanh((S_a - 70)/50)$, $\log(N_{sA0.1})$, and dN_1, in (38).

A world-wide map of the resulting universal kriging geoclimatic factor K_G is provided in Fig. 9.

B. ACCURACY OF THE UNIVERSAL KRIGING MODEL

As the universal kriging geoclimatic factor prediction error at known locations is minimised, a useful test of prediction accuracy requires the test location to be excluded from the matrix **G** of (35). This may be described as ''leave-one-location-out'' cross validation.

The results of this testing are shown in Table 5, comparing prediction error means and standard deviations with those of the existing ITU-R model [12]. A notable characteristic of these universal kriging results is the very low mean prediction error in all regions. None have magnitude exceeding 2.5 dB, and all regions with 15 or more link locations have mean error magnitude of 0.6 dB or less.

The use of universal kriging fading prediction can provide a significant benefit to regions of the world that are currently under-represented in the fading data, if they provide new fading data records, and the univesal kriging model is updated accordingly. As universal kriging uses interpolation of nearby data as well as regression, this local benefit is likely to be much greater than would be the case for a fading model that only uses OLS or GLS regression.

TABLE 5. Mean and standard deviation of prediction error by region, showing number of records, error statistics of the existing Rec. ITU-R P.530 model, and leave-one-location-out testing of the new universal kriging (UK) model.

Locations	P.530 mean	P.530 std dev	UK mean	UK std dev	Region
42	–0.96	4.94	–0.19	4.62	Western Europe
28	–0.37	5.48	+0.61	4.98	Scandinavia
16	+2.87	4.82	+0.43	4.82	Russia
5	–5.86	9.76	+1.53	7.59	Central Asia
5	+2.95	4.94	+2.48	5.59	South-East Canada
9	+5.75	4.93	–1.35	3.30	South-West Canada
4	–11.2	10.0	+1.80	11.1	Arctic Canada
6	+0.17	6.25	–0.29	6.37	Brazil
4	–1.38	6.27	–0.70	8.46	North-East Canada
1	+2.14	—	–2.36	—	Pakistan
7	–0.55	7.76	+0.54	5.88	Egypt
55	–0.49	6.13	–0.13	5.82	Southern Europe
3	–9.34	4.21	–0.43	5.86	Ghana
2	–1.47	5.87	+1.55	4.07	Senegal
3	+1.08	3.52	–1.38	3.76	South-East Africa
15	–9.83	7.27	+0.61	4.69	Cent-North Australia
31	–3.69	5.71	–0.32	5.87	South-East Australia
32	–6.02	6.52	+0.47	5.40	Southern Queensland
11	+0.57	5.60	–1.45	5.19	South-West Australia
7	–6.09	5.18	–0.49	4.59	Far North Queensland
535	–2.84	6.99	+0.052	5.37	All Regions

VI. CONCLUSION

We describe an empirical regression model for line-of-sight microwave link fading prediction that significantly improves prediction in some regions, such as Australia, where previously prediction accuracy was poor. This improvement is partly due to additional link fading observations, and partly due to new prediction parameters. Application of universal kriging to the solution of this problem is described for the first time, leading to even greater improvements in accuracy in regions with a good number of observations. Some parts

of the world are still under-represented in the fading data, particularly the Americas, Africa, and East Asia. The Australian experience has shown that this data can be generated at low cost, if the necessary data is available from installed radio equipment, and is collected and archived by the network management system, and some resources are allocated to processing the data. The universal kriging technique described here would see substantial design improvement for regions where this was done.

ACKNOWLEDGMENT

The authors would like to thank Dr. T. Tjelta for providing radio path profiles to accompany the earlier fading records in the ITU-R DBSG3 line of sight multipath fading data table. This enabled comparison of the new model with the alternative subrefractive diffraction loss approach, as well as a valuable validation check of existing records in the fading data table. We would also like to thank Telstra Corporation radio transmission staff and their equipment vendors, for their dedication to the principle of network monitoring and data archiving, that enabled the production of the large number of Australian radio link fading distributions, contributed to the ITU-R DBSG3 data table.

APPENDIX A FADING DATA FROM DIGITAL LINKS

A brief description is provided here of the procedure used in Australia [20], [31], to produce average year worst-month fading distributions from installed radio links.

1) Identify line-of-sight links, with automatic transmit power control disabled, where minimum and maximum receive level data is continuously available for every 15 minutes, over a period of one or more years.
2) Process the data, estimating the receive level distributions for each 15 minute period, and accumlate these into monthly distributions. If only the 15 minute minimum and maximum levels are known, assume a uniform voltage distribution between those limits for each 15 minute period [31], but use any additional data; most Australian links also reported time below 4 levels.
3) Plot the receive level time series of fading months, to check that apparent fading is not equipment related. These plots include rain data from nearby weather stations, to ensure fading events are not rain related.
4) Each percentage point in the worst month distribution for the year is taken to be the worst case at that percentage point for the fading months. If more than one year of data is available, take the dB mean as the average year worst month distribution.
5) The Australian data is from 6 to 24 MHz bandwidth systems, but the fading distribution for a very narrow bandwidth system is required, having an approximate Rayleigh 10 dB per decade deep fading tail slope. Digital radio systems with finite bandwidths typically have an initial fading distribution tail slope around 10 dB per decade, but then reducing slope at the smallest percentages of time. This <10 dB per decade tail region is ignored, as not representative of narrow band fading.

REFERENCES

[1] K. W. Pearson, "Method for the prediction of the fading performance of a multisection microwave link," *Proc. Inst. Electr. Eng.*, vol. 112, no. 7, pp. 1291–1300, 1965.
[2] K. Morita, "Prediction of Rayleigh fading probability of line-of sight microwave links," *Rev. Elec. Commun. Labs, NTT Corp.*, vol. 18, pp. 810–821, Nov.-Dec. 1970.
[3] *Propagation Data and Prediction Methods Required for Line-of-Sight Radio-Relay Systems*, Int. Telecommun. Union, Geneva, Switzerland, 1990.
[4] W. T. Barnett, "Multipath propagation at 4, 6, and 11 GHz," *Bell Syst. Tech. J.*, vol. 51, no. 2, pp. 321–361, Feb. 1972.
[5] A. Vigants, "Space-diversity engineering," *Bell Syst. Tech. J.*, vol. 54, no. 1, pp. 103–142, Jan. 1975.
[6] *Propagation data and prediction methods required for line-of-sight radio-relay Systems*, Int. Telecommun. Union, Geneva, Switzerland, 1999. [Online]. Available: https://www.itu.int/rec/R-REC-P.530-8-199910-S/en
[7] R. L. Olsen and T. Tjelta, "Worldwide techniques for predicting the multipath fading distribution on terrestrial LOS links: Background and results of tests," *IEEE Trans. Ant. Prop*, vol. 47, no. 1, pp. 157–170, Jan. 1999.
[8] R. L. Olsen, T. Tjelta, L. Martin, and B. Segal, "Worldwide techniques for predicting the multipath fading distribution on terrestrial LOS links: Comparison with regional techniques," *IEEE Trans. Antennas Propag.*, vol. 51, no. 1, pp. 23–30, Jan. 2003.
[9] B. Bean, "The radio refractive index of air," *Proc. IRE*, vol. 50, no. 3, pp. 260–273, Mar. 1962.
[10] J. M. Rueger, "Refractive index formulae for radio waves," in *Proc. Int. Fed. Surveyors*, Washington DC, USA, Apr. 2002, pp. 19–26.
[11] L. Boithias and J. Battesti, "Protection contre les vanouissements sur les faisceaux Hertziens en visibilit (Protection against fading on line-of-sight radio paths)," *Annales Telecommun.*, vol. 22, nos. 9–10, pp. 230–242, 1967.
[12] *Propagation Data and Prediction Methods Required for Line-of-Sight Radio-Relay Systems*, Int. Telecommun. Union, Geneva, Switzerland, Dec. 2017. [Online]. Available: https://www.itu.int/rec/R-REC-P.530-17-201712-I/en
[13] G. Shepherd, "East-west 6.7 GHz propagation study," Telecom Australia Radiocom Branch, Melbourne, Australia, Tech. Rep.9/79, Jun. 1979.
[14] R. Harvey, "A subrefractive fading model for microwave paths using surface synoptic meteorological data," *IEEE Trans. Antennas Propag.*, vol. 35, no. 7, pp. 832–844, Jul. 1987.
[15] J. A. Schiavone, "Prediction of positive refractivity gradients for line-of-sight microwave radio paths," *Bell Syst. Tech. J.*, vol. 60, no. 6, pp. 803–822, Jul. 1981.
[16] A. Vigants, "Microwave radio obstruction fading," *Bell Syst. Tech. J.*, vol. 60, no. 6, pp. 785–801, Jul. 1981.
[17] A. M. Obukhov, "Turbulence in an atmosphere with a non-uniform temperature," *Boundary-Layer Meteorol.*, vol. 2, no. 1, pp. 7–29, 1971.
[18] S. J. Salamon, H. J. Hansen, and D. Abbott, "Modelling radio refractive index in the atmospheric surface layer," *Electron. Lett.*, vol. 51, no. 14, pp. 1119–1121, Jul. 2015.
[19] G. Kizer, "Improvements in fixed point-to-point microwave radio path design," in *Proc. Wireless Telecomun. Symp.*, Pomona, CA, USA, Apr. 2008, pp. 354–359, doi: 10.1109/wts.2008.4547588.
[20] *New Source of Measured Data for ITU-R Study Group 3 Databank Table I-2, Line-of-Sight Average Worst-Month Multipath Fading and Enhancement in Narrow Bandwidths*, document 3M/186, Geneva, Switzerland, Oct. 2011.
[21] A. E. Barrios, "A terrain parabolic equation model for propagation in the troposphere," *IEEE Trans. Antennas Propag.*, vol. 42, no. 1, pp. 90–98, Jan. 1994.
[22] D. J. Donohue and J. R. Kuttler, "Propagation modeling over terrain using the parabolic wave equation," *IEEE Trans. Antennas Propag.*, vol. 48, no. 2, pp. 260–277, Feb. 2000.
[23] C. M. Ewenz, A. S. Kulessa, and S. J. Salamon, "Using mesoscale models together with PEM propagation models to determine microwave link output," in *Proc. URSI Climpara*, pp. 89–92, May 2001.
[24] J. Claverie, "Vertical refractivity profiles within the marine surface boundary layer," *Proc. EuCAP*, Krakow, Poland, Mar./Apr. 2019. [Online]. Available: https://ieeexplore.ieee.org/abstract/document/8740060
[25] *Testing the new ERA-Interim surface refractivity gradient distribution maps, proposed for Recommendation ITU-R*, document 453 3J/76, Geneva, Switzerland, Aug. 2014.

[26] T. Tjelta, T. G. Hayton, B. Segal, and E. L. Salonen, "Correlation of observed multipath occurrence with climatic parameters derived from radiosondes, surface stations, and numerical atmosphere models," in *Proc. URSI Climpara*, Ottawa, Canada, 1998, pp. 85–97.
[27] *Acquisition, Presentation and Analysis of Data in Studies of Radiowave Propagation*, Int. Telecommun. Union, Geneva, Switzerland, Dec. 2017. [Online]. Available: https://www.itu.int/rec/R-REC-P.311-17-201712-I/en
[28] T. Tjelta, R. L. Olsen, and L. Martin, "Systematic development of new multivariable techniques for predicting the distribution of multipath fading on terrestrial microwave links," *IEEE Trans. Antennas Propag.*, vol. 38, no. 10, pp. 1650–1665, Oct. 1990.
[29] *Propagation Data and Prediction Methods Required for Line-of-Sight Radio-Relay Systems*, Int. Telecommun. Union, Geneva, Switzerland, 2001. [Online]. Available: https://www.itu.int/rec/R-REC-P.530-9-200102-S/en
[30] *Propagation Data and Prediction Methods Required for Line-of-Sight Radio-Relay Systems*, Int. Telecommun. Union, Geneva, Switzerland, Oct. 2009. [Online]. Available: https://www.itu.int/rec/R-REC-P.530-13-200910-S/en
[31] *New Australian Data for DBSG3 Table I-2 Line-of-Sight Average Worst-Month Multipath Fading and Enhancement in Narrow Bandwidths*, ITU-R Working Party input, Geneva, Switzerland, Jun. 2016.
[32] S. J. Salamon, H. J. Hansen, and D. Abbott, "Radio link clear-air fading prediction from surface weather station data," in *Proc. ISAP*, Okinawa, Japan, Oct. 2016, pp. 72–73.
[33] S. J. Salamon, H. J. Hansen, and D. Abbott, "How real are observed trends in small correlated datasets?" *Roy. Soc. Open Sci.*, vol. 6, no. 3, Mar. 2019, Art. no. 181089.
[34] M. Grabner, V. Kvicera, P. Pechac, M. Kvicera, P. Valtr, and A. Martellucci, "World maps of atmospheric refractivity statistics," *IEEE Trans. Antennas Propag.*, vol. 62, no. 7, pp. 3714–3722, Jul. 2014.
[35] Global Hourly Data. *National Oceanic and Atmospheric Administration*. Accessed: Aug. 11, 2019. [Online]. Available: http://ftp.ncdc.noaa.gov/pub/data/noaa
[36] N. A. C. Cressie, "Spatial prediction and kriging," in *Statistics for Spatial Data*. New York, NY, USA: Wiley, 1993, pp. 105–210.
[37] G. Matheron, "Principles of geostatistics," *Econ. Geol.*, vol. 58, no. 8, pp. 1246–1266, Dec. 1963.
[38] N. A. C. Cressie, "Geostatistics," in *Statistics for Spatial Data*. New York, NY, USA: Wiley, 1993, pp. 29–104.
[39] M. Sambridge, J. Braun, and H. McQueen, "Geophysical parametrization and interpolation of irregular data using natural neighbours," *Geophys. J. Int.*, vol. 122, no. 3, pp. 837–857, Dec. 1995.
[40] I. Todhunter, "Area of a spherical triangle. Spherical excess," in *Spherical Trigonometry*, 5th ed. London, U.K.: Macmillan, 1886, pp. 71–80. [Online]. Available: http://www.gutenberg.org/ebooks/19770
[41] N. A. C. Cressie, "Special topics in statistics for spatial data," in *Statistics for Spatial Data*. New York, NY, USA: Wiley, 1993, pp. 277–379.
[42] D. Shepard, "A two-dimensional interpolation function for irregularly-spaced data," in *Proc. 23rd ACM Nat. Conf.*, 1968, pp. 517–524.
[43] C. J. Willmott, C. M. Rowe, and W. D. Philpot, "Small-scale climate maps: A sensitivity analysis of some common assumptions associated with grid-point interpolation and contouring," *Amer. Cartographer*, vol. 12, no. 1, pp. 5–16, Jan. 1985.
[44] *Guide to the application of the propagation methods of Radiocommunication Study Group 3*, Int. Telecommun. Union, Geneva, Switzerland, Dec. 2017. [Online]. Available: https://www.itu.int/rec/R-REC-P.1144-9-201712-I/en
[45] *Propagation by Diffraction*, Int. Telecommun. Union, Geneva, Switzerland, Jan. 2018. [Online]. Available: https://www.itu.int/rec/R-REC-P.526-14-201801-I/en

STEPHEN J. SALAMON (Member, IEEE) was born in Adelaide, Australia, in 1954. He received the B.Sc. degree in physics and computing science and the B.E. degree in electrical and electronic engineering from The University of Adelaide, in 1976 and 1981, respectively, where he is currently pursuing the Ph.D. degree with the School of Electrical and Electronic Engineering, researching clear-air terrestrial radio fading, under D. Abbott and H. J. Hansen. Initially an FM Broadcast Station Engineer, in late 1981, he joined Telecom Australia as a Radio Link Design Engineer, designing both digital and analog systems from VHF single channel to broadband microwave digital. From 1985 to 1992, he designed systems in remote regions of Australia for the Rural and Remote Areas Program. In 1995, he joined Telstra Corporation Operations, as a Principal Engineer with the National Leadhouse Radio Group. Since 1998, he has been an Active Member of the Australian Radio Study Group 3, drafting many Australian inputs to the Working Parties of ITU-R Study Group 3 (radiowave propagation). He has been an Australian Delegate to these meetings, since 2008, contributing to the development of prediction models for terrain diffraction, interference propagation, and terrestrial link design. He is currently the Chairman of the Australian Radio Study Group 3 (Radiowave Propagation).

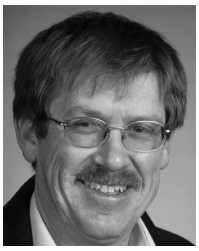

HEDLEY J. HANSEN (Member, IEEE) was born in Port Elizabeth, South Africa, in 1957. He received the B.Sc. (Hons.), M.Sc. *(cum laude)*, and Ph.D. degrees from the University of Natal, Durban, South Africa, in 1980, 1983, and 1988, respectively. His Ph.D. research, under M. W. J. Scourfield, was concerned with magnetospheric wave particle interaction processes that give rise to the optical aurora. In 1988, he joined the Space Plasma Waves Group, The University of Newcastle, Australia, as a Postdoctoral Research Associate. The group maintained arrays of induction magnetometers in Australian Antarctic Territory and across the Australian Mainland. He moved to the RF Technology Group, Electronic Warfare and Radar Division, Defence Science and Technology Organisation, Edinburgh, Australia, in 1996, as a Senior Research Scientist. His professional interests lie in RF remote sensing at millimeter and submillimeter wavelengths, microstrip antenna design, phased array and miniaturized radar technologies, and radiowave propagation. He is currently an Adjunct Senior Lecturer with The University of Adelaide. He is a member of American Geophysical Union and Australian Institute of Physics.

DEREK ABBOTT (Fellow, IEEE) was born in South Kensington, London, U.K., in 1960. He received the B.Sc. degree (Hons.) in physics from Loughborough University, Leicestershire, U.K., in 1982, and the Ph.D. degree in electrical and electronic engineering from The University of Adelaide, Adelaide, Australia, in 1995, under K. Eshraghian and B. R. Davis. From 1978 to 1986, he was a Research Engineer at the GEC Hirst Research Centre, London, U.K. From 1986 to 1987, he was a VLSI Design Engineer at Austek Microsystems, Australia. Since 1987, he has been with The University of Adelaide, where he is currently a Full Professor with the School of Electrical and Electronic Engineering. He coedited *Quantum Aspects of Life* (Imperial College Press, 2008), coauthored *Stochastic Resonance*, (Cambridge University Press, 2008), and coauthored *Terahertz Imaging for Biomedical Applications*, (Springer-Verlag, 2012). His interest is in the area of multidisciplinary physics and electronic engineering applied to complex systems. His research programs span a number of areas, including networks, game theory, energy policy, stochastics, and biophotonics. He is a Fellow of the Institute of Physics (IOP) and the Institute of Electrical & Electronic Engineers. He has won a number of awards, including the South Australian Tall Poppy Award for Science, in 2004, the Australian Research Council (ARC) Future Fellowship, in 2012, the David Dewhurst Medal, in 2015, the Barry Inglis Medal, in 2018, and the M. A. Sargent Medal, in 2019, for eminence in engineering. He has served as an Editor and/or a Guest Editor for a number of journals, including the IEEE JOURNAL OF SOLID-STATE CIRCUITS, the *Journal of Optics B* (IOP), *Microelectronics Journal* (Elsevier), *Chaos* (AIP), *Smart Structures and Materials* (IOP), *Fluctuation Noise Letters* (World Scientific), *PLOS ONE*, PROCEEDINGS OF THE IEEE, and the PHOTONICS JOURNAL (IEEE). He is currently on the Editorial Boards of *Scientific Reports* (Nature), IEEE ACCESS, and *Royal Society Open Science*. He is also the Editor-in-Chief (EIC) of IEEE ACCESS and serves on the IEEE Publication Services and Products Board (PSPB).